3D Dirac semimetals supported tunable hybrid plasmonic terahertz waveguides with a dielectric wedge

Qi Wang[1](王淇), Longhao Lai[1](赖隆浩), Ying Liang[1](梁莹), Haitao Zhang[1](张海韬), Mingyang Chen[1](陈明阳), Zijie Dai[1*](戴子杰), Juncheng Cao[2*](曹俊诚)

[1] *School of Mechanical Engineering, Jiangsu University, Zhenjiang 212013, China*

[2] *State Key Laboratory of Materials for Integrated Circuits, Shanghai Institute of Microsystem and Information Technology, Chinese Academy of Sciences, Shanghai 200050, China*

*Corresponding author: daizijie@ujs.edu.cn jccao@mail.sim.ac.cn

Abstract

A novel design of tunable hybrid plasmonic waveguide in the terahertz (THz) regime is present based on three-dimensional Dirac semimetals (3D DSM) with wedge-shaped structure. The propagation characteristics at a broad band from 0.5 THz to 3.3 THz are systematically investigated considering the structural parameters and Fermi energy of DSM, in terms of the normalized mode area, propagation length, figure of merit, and mode field distributions. By tuning the Fermi energy of DSM from 0.03 eV to 0.15 eV, the propagation length of the hybrid plasmonic waveguides could be effectively modulated with a modulation depth more than 95%. The crosstalk between adjacent waveguides is evaluated by analyzing the symmetric/anti-symmetric modes coupling process, which demonstrates the effective crosstalk suppression requires a minimum center-to-center separation of 60 μm. These results not only provide valuable insights for understanding the propagation mechanism of 3D DSM hybrid plasmonic waveguides, but also open new avenues for the applications of tunable and broadband THz waveguides devices.

Key words: Terahertz waveguide, Dirac semimetal, hybrid plasmonic, tunable

1. Introduction

Terahertz (THz) waves typically refer to electromagnetic waves with a frequency of 10^{11} Hz to 10^{13} Hz, which are between microwaves and infrared waves in the electromagnetic spectrum spanning the transition region between electronics and photonics [1]. THz waves exhibit a set of distinctive merits, e.g. high penetration depth,

low photon energy, broad bandwidth, and fingerprint spectral characteristics [2,3]. Owing to these unique properties, THz waves are highly promising for applications in non-destructive testing, biosensing, and next-generation high-speed wireless communications [4-7]. Suitable waveguides structures can confine and guide THz waves within a well-defined region, achieving efficient coupling between devices and mitigating the environmental susceptibility inherent to free-space propagation. As key components for THz application fields, the performance of terahertz waveguides directly determines the transmission efficiency of terahertz systems [8].

According to guiding mechanisms, THz waveguides can be divided into dielectric waveguides, photonic crystal waveguides, anti-resonant waveguides [1] and surface plasmonic waveguides [9]. Among them, surface plasmonic waveguides excite surface plasmon polariton (SPP) through electron oscillations at the interface between metal and dielectric, which reduce the mode area and break the diffraction limit [10-11]. For instance, Gadalla et al. fabricated low-loss titanium-nitride (TiN) thin film on MgO substrate and imaged the generated SPPs in the mid-infrared regime to determine the mode wavelength and propagation length [12]. Cui et al. excited SPPs on the Mo surface by etching a grating structure on a single-crystal Mo microrod structure, which had a long propagation length and low transmission loss in the near-infrared band [13]. However, for a traditional metallic plasmonic waveguide, the characteristics of the supported plasmonic mode are inherently fixed once the geometric configuration is determined, making it difficult to meet the tunable requirements of practical applications. In related studies, Deng et al. demonstrated the electrical and all-optical tunability of photonic Dirac points in graphene-based photonic superlattices and examined their robustness against structural disorder [14,15]. In recent years, tunable hybrid plasmonic waveguides have attracted widespread attention due to their low loss and tunable properties, particularly those based on graphene. Kou et al. further demonstrated that hybrid plasmonic waveguides can combine low propagation loss with subwavelength confinement, providing a route

toward compact photonic integration [16]. Huang et al. demonstrated long-distance, strongly confined THz propagation by embedding graphene within a slot waveguide positioned between metallic wires [17]. Yuan et al. designed a double-layer graphene Si slot waveguide modulator and adjusted the transmission characteristics of the THz signal by changing the chemical potential of graphene, and the propagation length modulation range reached 300 μm [18].

Although two-dimensional material hybrid plasmonic waveguides represented by graphene have achieved certain progress, the inherently low absorption of incident electromagnetic waves and weak coupling strength of graphene would inevitably constrain both the tunability and the geometric design flexibility of such waveguides. Three-dimensional Dirac semimetals (3D DSMs), overcoming the aforementioned intrinsic limitations of two-dimensional counterparts, offer an ultrahigh electron mobility up to 9×10^6 cm^2 V^{-1} s^{-1} and superior environmental stability, thereby presenting an excellent platform for the construction of high-performance THz functional devices [19-22]. In 2021, Dai et al. experimentally demonstrated that a Cd_3As_2 thin film retains high electron mobility within the THz band and are capable of supporting the excitation and propagation of surface plasmon polaritons [23]. Cheng et al. systematically investigated the temperature-tunable transmission characteristics of 3D DSM-based hybrid plasmonic waveguides in the THz regime and elucidated their relationship with the transition frequency, thereby substantiating the feasibility of employing 3D DSMs for tunable hybrid plasmonic waveguides [11].

In this paper, we proposed a novel hybrid plasmonic THz waveguide based on wedge-shaped structure, in which the 3D DSM excites SPP modes and a cylindrical Si waveguide conveys dielectric modes. The resulting hybrid plasmonic mode simultaneously exhibits strong mode confinement and extended propagation length. The influence factors of propagation characteristics were systematically interpreted from the perspectives of structure parameters and Fermi energy of DSM. The results show that the propagation length can be dynamically tuned over a broad range by

varying the Fermi energy of the 3D DSM, achieving a modulation depth exceeding 95%. In addition, the crosstalk between adjacent waveguides was evaluated by means of modes analysis to pursue an integrated and parallel THz guiding. The outcomes demonstrate that the proposed waveguide structure holds significant potential for the development of high-performance integrated terahertz functional devices.

2. Structure design and 3D DSM modeling

Fig. 1 illustrates the proposed hybrid plasmonic THz waveguide based on 3D DSM. A DSM layer of thickness h_1=10 μm is deposited on a hybrid Si/SiO_2 substrate composed of a buried SiO_2 layer (h_2=2 μm) and a bottom high-resistivity Si layer (h_3=4 μm). The dielectric ridge consists of a cylindrical Si fiber, a wedge-shaped Si segment, and is embedded in a SiO_2 cladding. The parameters r, g, d, and H=3μm denote the fiber radius, separation gap, wedge length, and wedge height, respectively. The relative permittivities of Si and SiO_2 are 11.7 and 3.9, respectively. In the simulation, the cladding is modeled as a semi-infinite background with PML boundaries. Based on the designed waveguide, the THz waves are well confined in the gap between the Si fiber and the wedge-shaped Si that propagates along the z-axis direction. By tuning the Fermi energy of the 3D DSM via an external bias voltage V_g, the transmission characteristics of the hybrid mode can be flexibly regulated [24].

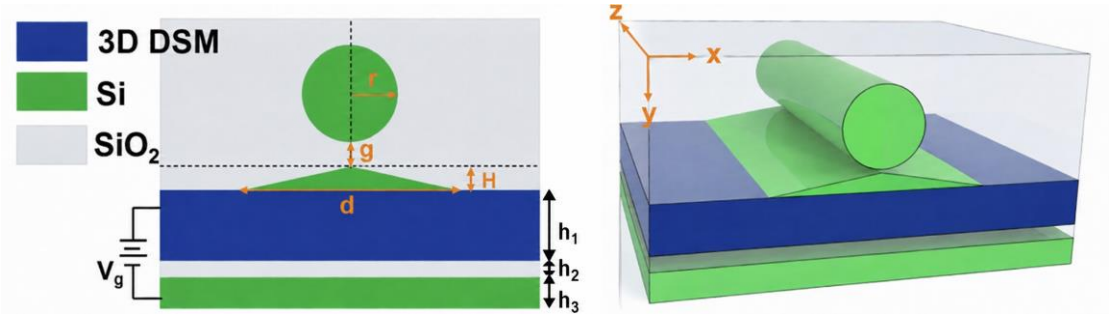


Fig. 1 Structural diagrams of the proposed hybrid plasmonic THz waveguide.

The complex conductivity of the 3D DSM can be defined using the Kubo formula, described as follows [25]:

$$\mathrm{Re}\left(\sigma(\Omega)\right)=\frac{e^2 g k_F}{24\hbar\pi}\Omega\theta(\Omega-2) \tag{1}$$

$$\mathrm{Im}(\sigma(\Omega)) = \frac{e^2 g k_F}{24\hbar\pi^2}\left[\frac{4}{\Omega} - \Omega\ln\left(\frac{4\varepsilon_c^2}{|\Omega^2-4|}\right)\right] \tag{2}$$

in which $k_F=E_F/\hbar v_F$, $\hbar$ is the reduced Planck constant, e is the elementary charge, E_F denotes the Fermi energy, $v_F=1\times10^6$ m/s is the Fermi velocity, $\varepsilon_c=3$, $\Omega=\hbar\omega/E_F+i\hbar\tau^{-1}/E_F$, and $\theta(\Omega\text{-}2)$ represents the low-temperature limit ($T<<E_F$) approximation of $G(\Omega/2)$, with $G(E)=n(-E)-n(E)$, $n(E)$ being the Fermi-Dirac distribution function, $g=40$ the degeneracy factor, and $\tau=4.5\times10^{-13}$ s the intrinsic relaxation time.

Further, the complex permittivity of the 3D DSM can be described using a two-band model accounting for interband transition, which is expressed as [26]:

$$\varepsilon = \varepsilon_b + i\sigma/\omega\varepsilon_0 \tag{3}$$

where $\varepsilon_b=1$ denotes the background relative permittivity and ε_0 the vacuum permittivity. σ represents the complex conductivity of the 3D DSM, calculated by Eqs. (1) and (2). The real and imaginary parts of the permittivity of 3D DSM at various Fermi energy are shown in Fig. 2. It is evident that the absolute values of Re(ε) and Im(ε) increase markedly with E_F, and both of them approach zero as the frequency increases, signifying a transition of the 3D DSM from a metallic to a dielectric electromagnetic response [27]. Leveraging the above material model, the propagation characteristics of terahertz waves within the waveguide are analyzed using the finite element method.

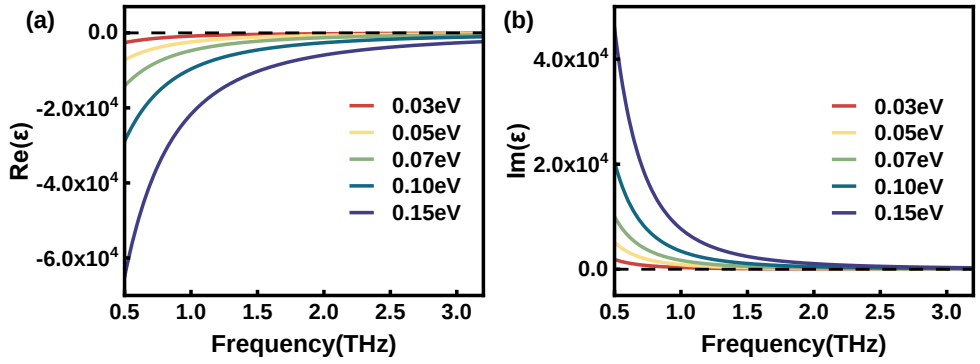


Fig. 2 Fermi energy dependent dielectric constant of 3D DSM: (a) Real part. (b) Imaginary part.

3. Results and Discussion

The propagation characteristics of the hybrid surface plasmonic mode are

dominated by the interaction between the low-loss dielectric mode and the strongly confined plasmonic mode. Consequently, we examine these two constituent modes individually before analyzing the hybrid mode within the THz waveguide. First, the situation in which only the dielectric mode propagates in the waveguide without the plasmonic mode is taken into account. Fig. 3(a) shows the real part of the effective mode index of the dielectric mode as a function of the Si fiber radius, and Re(n_{eff}) increases monotonically with the increase of radius, indicating that the hybrid mode energy becomes more tightly confined within the cylindrical Si fiber. Nevertheless, the enhancement of mode confinement gradually saturates as the radius continues to increase. Fig. 3(b) illustrates the electric-field distribution within the substrate when only the plasmonic mode is supported. The field propagates through both the Si and SiO_2 layers of the substrate, and its intensity weakens with increasing Fermi energy, while the spatial profile of the plasmonic mode remains nearly invariant across the examined Fermi energy.

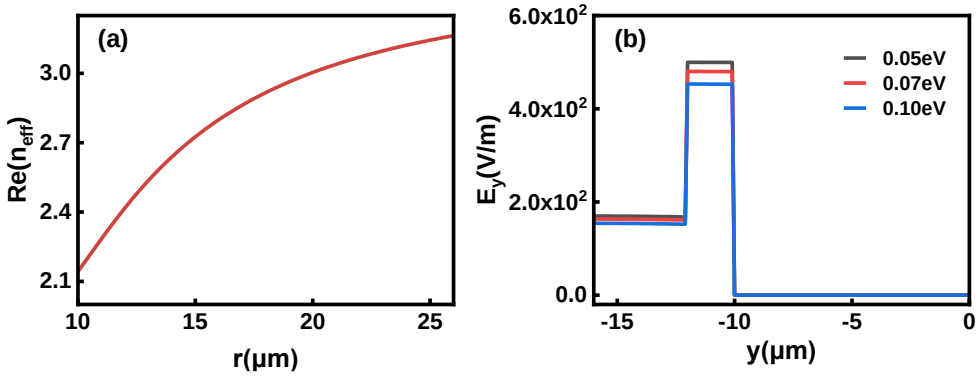


Fig.3 (a) The effective mode refractive index of dielectric mode as a function of the radius (r) of cylindrical Si. (b) The electric field intensity distribution of plasmonic mode versus E_F.

Fig. 4 shows the mode field distributions for the dielectric and plasmonic modes under various conditions. As the dielectric radius increases, the energy of the dielectric mode becomes more tightly confined within the cylindrical Si fiber, accompanied by a shorter evanescent tail. The electric-field energy of the SPP mode is almost entirely localized within the Si and SiO_2 layers of the substrate, with the majority concentrated in the SiO_2 layer adjacent to the 3D DSM. Moreover, the field

profiles reveal that the plasmonic mode induces a highly localized electric field on the 3D DSM surface, thereby providing a certain degree of field enhancement for the incident wave.

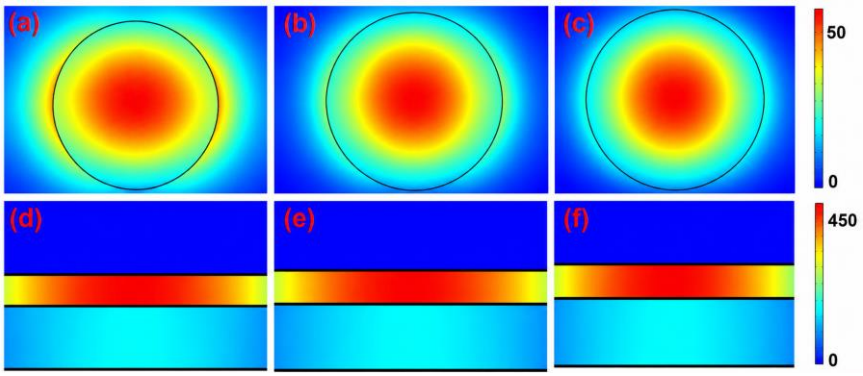


Fig.4 (a)-(c) The dielectric mode field distributions at r=15, 20, and 25 μm. (d)-(f) The plasmonic mode field distributions at E_F=0.05, 0.07, and 0.1 eV.

After individually characterizing the dielectric and plasmonic modes, the propagation properties of the hybrid plasmonic mode supported by the proposed waveguide are further investigated, beginning with the influence of distinct wedge geometries. Fig. 5 describes the dependence of the hybrid plasmonic mode properties on the wedge geometry, rectangular, elliptical, and triangular profiles, respectively. As illustrated in Fig. 5(a), the real part of the effective mode index increases monotonically with d, indicating that extending the wedge length gradually enhance the confinement of the hybrid mode within the waveguide, and then tend to be saturated. In addition to the effective mode index, the normalized mode area, propagation length, and figure of merit (FOM) are also essential parameters for evaluating the characteristics of the hybrid plasmonic mode. For the hybrid-mode analysis that follows, all reported modal quantities refer specifically to the fundamental hybrid plasmonic mode.

During the actual propagation process, the distribution of electromagnetic field energy in the waveguide is also a vital factor. The normalized effective mode area A_m/A_0 is defined to reflect the mode

confinement capability of the waveguide, where $A_0=\lambda^2/4$ is the diffraction-limited area, A_m can be expressed as [28]:

$$A_m = \frac{w_m}{\max\{w(r)\}} = \frac{1}{\max\{w(r)\}} \iint_{-\infty}^{+\infty} w(r) d^2 r \tag{4}$$

where w_m denotes the total electromagnetic energy in the waveguide, and $w(r)$ represents the energy density that could be calculated by:

$$w(r) = \frac{1}{2}\left(\frac{d(\varepsilon(r)\omega)}{d\omega}|E(r)|^2 + \mu_0 |H(r)|^2\right) \tag{5}$$

The propagation length, defined as the distance over which the electromagnetic energy decays to $1/e$ of its initial value, serves as a key metric for evaluating transmission loss. It is expressed as:

$$L_{sp} = \frac{\lambda}{4\pi \,\mathrm{Im}(n_{eff})} \tag{6}$$

Where $n_{\mathrm{eff}}=\beta/k_0$ denotes the effective mode index, β is the complex propagation constant，k_0 is the free-space wavenumber, $\mathrm{Im}(n_{\mathrm{eff}})$ is the imaginary part of the effective mode index.

The figure of merit (FOM) is employed to quantify the trade-off between propagation length and mode confinement, and is defined as:

$$FOM = \frac{L_{sp}}{\sqrt{A_m}} \tag{7}$$

The changes of the normalized effective mode area, propagation length, and FOM are shown in the Figs. 5(b)-(d). As d increases, the effective mode area, propagation length, and FOM decrease gradually with the enhanced interaction between the SPP mode and the dielectric mode. In addition, the wedge geometry plays a non-negligible role; distinct wedge profiles yield different coupling efficiencies between the SPP and dielectric mode, leading to variations in the characteristic parameters, with the coupling strength decreasing in the order rectangular, elliptical, and triangular.

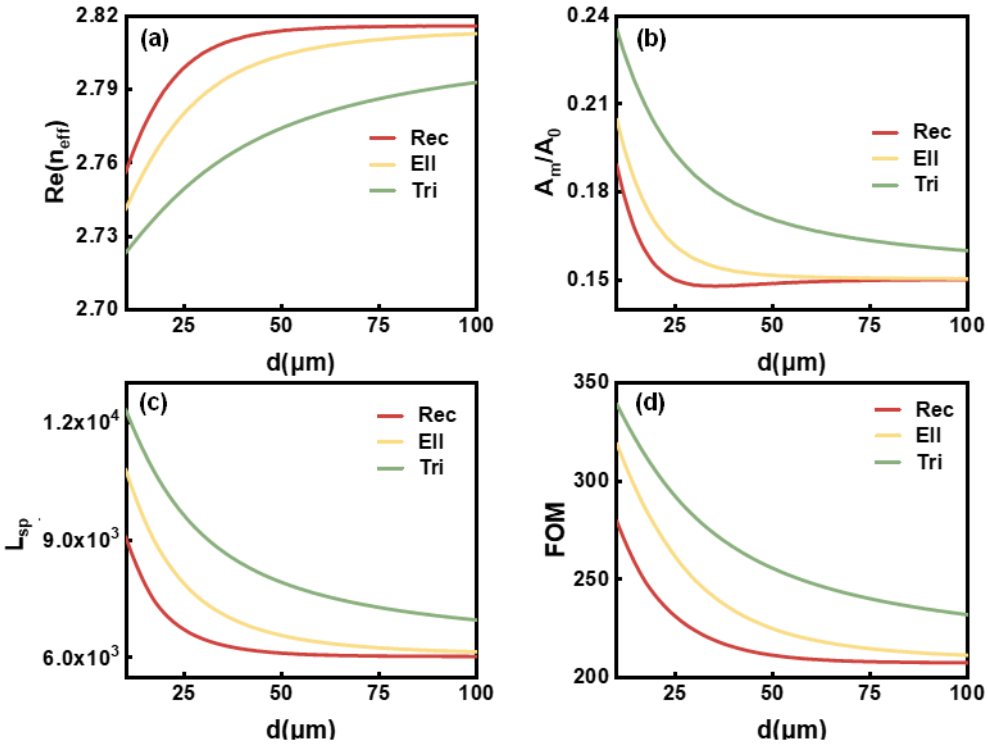


Fig.5 The wedge length (*d*) dependent propagation parameters with different wedge structures: (a) The real part of effective mode refractive index. (b) Normalized mode area. (c) propagation length, (d) Figure of merit (FOM).

Fig. 6 presents the mode field distributions of the hybrid mode under various conditions. For a fixed wedge length, Figs. 6(a)-(c) exhibit effective mode index of $2.76+1.30\times10^{-3}$i, $2.74+1.10\times10^{-3}$i, and $2.72+9.68\times10^{-4}$i, respectively, indicating that enhanced coupling between the hybrid mode and the dielectric ridge simultaneously strengthens mode confinement and introduces additional propagation loss. Figs. 6(d)-(f) depict the hybrid plasmonic mode profiles at d=100 μm. As d increases, the coupling between the SPP mode and dielectric mode also increases, leading to a redistribution of the mode field within the respective shaped coupling regions. Optimal coupling between the two modes is achieved around d≈50 μm. Further increases in d yield only marginal variations in the waveguide transmission characteristics, as evidenced by the progressively flattened trends in Fig. 5. Larger wedge lengths also attenuate the influence of wedge geometry on the propagation properties. For example, Figs. 6(d)-(f) yield effective mode indices of $2.81+1.99\times10^{-3}$

i, 2.80+1.95×10^{-3}i, and 2.79+1.72×10^{-3}i, respectively.

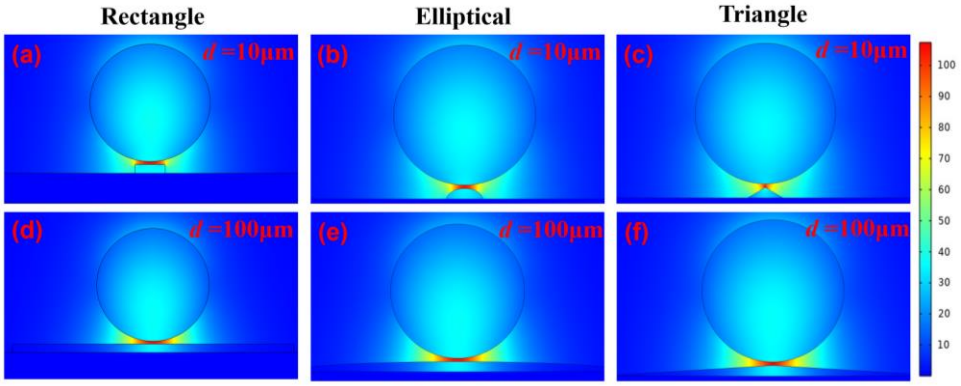


Fig.6 Mode field distributions (2 THz, E_F=0.1 eV) for different wedge structures of rectangle, elliptical and triangle at: (a)-(c) d=10μm. (d)-(f) d=100μm.

To further understand the influence of wedge geometry and length on the propagation characteristics of the hybrid plasmonic waveguide based on 3D DSM. Fig. 7 presents the one-dimensional electric-field energy distributions of the hybrid mode at selected positions (indicated by the dashed lines in Fig. 1) under various conditions. Along the x-direction, the electric-field energy broadens at the symmetry center and its peak magnitude increases with d, the degree of energy confinement in this direction follows the order: triangular > elliptical > rectangular, which is consistent with the mode intensity profiles. The distribution of electric field energy in the y direction is somewhat different. Specifically, different lengths and shapes have almost no effect on the distribution profile of the electric field energy. The hybrid mode is mainly concentrated in the gaps (SiO_2) of the dielectric ridges, and some hybrid mode energy is also carried out in the Si dielectric.

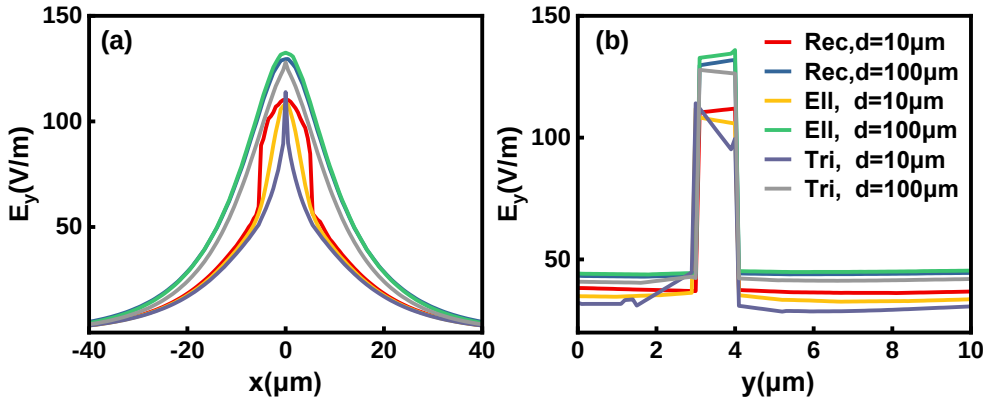


Fig.7 Electric field intensity distribution along: (a) The x-direction at y=3 μm. (b) The y-direction at x=0 μm.

The above analysis indicates that the hybrid mode is predominantly confined within the SiO_2 spacer separating the cylindrical and wedge-shaped Si segments; hence, it is imperative to examine the influence of frequency and the gap height on the waveguide propagation characteristics. Taking the triangular wedge as an example, Fig. 8 illustrates the effect of varying the gap height between the Si fiber and the wedge (0.5 μm, 1 μm, 5 μm) on the hybrid-mode characteristics. The real part of the effective mode index increases with frequency because the permittivity of the 3D DSM decreases, driving a transition from metallic to dielectric behavior and weakening its plasmonic response, which in turn causes the mode to leak into the DSM. Overall, both the normalized mode area and the propagation length exhibit an increasing trend, as depicted in Figs. 8(b) and 8(c). At low frequencies, however, the normalized mode area and propagation length initially decrease with increasing frequency; this is attributed to the longer THz wavelength, which imposes weaker confinement and allows the hybrid mode to extend into other regions of the waveguide. As the frequency continues to increase, the reduced wavelength enables the hybrid mode to be tightly concentrated within the gap, thereby decreasing both the normalized mode area and the propagation length. Upon further frequency increase, the plasmonic response of the 3D DSM diminishes, and the low-loss dielectric mode gradually prevails, leading to an increase in both the normalized mode area and the propagation length. This evolution is also reflected in Fig. 8(d), where a higher FOM signifies a larger contribution of the dielectric mode within the hybrid mode.

The height of the gap between the Si wedge and fiber exerts a pronounced influence on the propagation characteristics. An increase in the gap height leads to a smaller real part of the effective mode index and a concomitant increase in the normalized mode area. This occurs because increasing the gap weakens the confinement of the hybrid mode and shifts the mode toward low-loss dielectric-like

characteristics, as illustrated in Figs. 8(a) and 8(b). For the same reason, both the propagation length and the figure of merit rise with increasing gap height, as shown in Figs. 8(c) and 8(d).

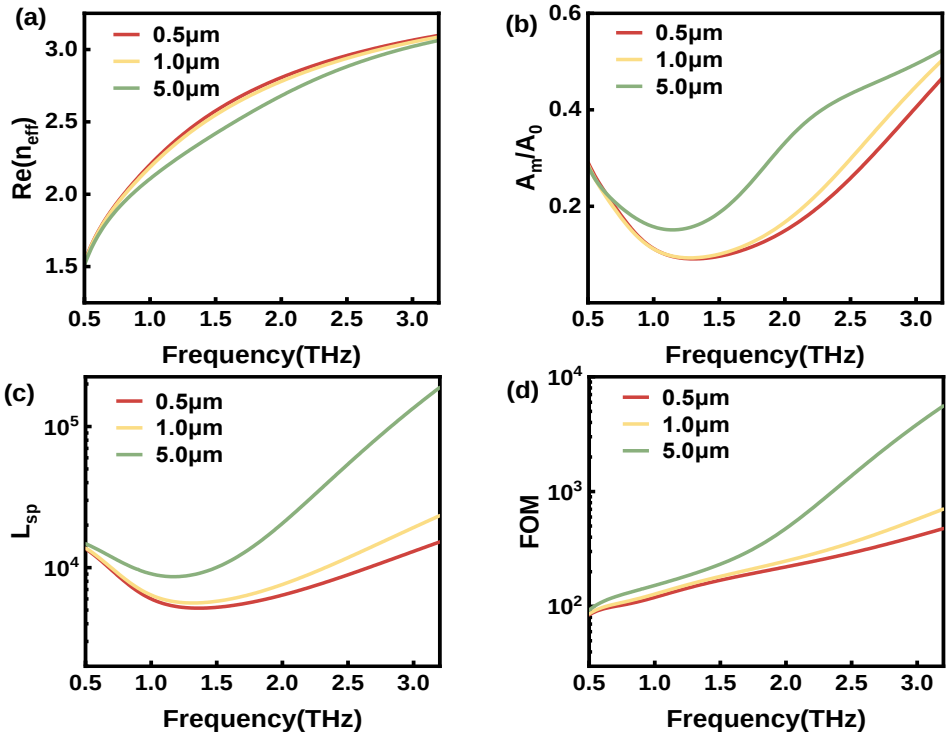


Fig.8 The separation (g) between the fiber and the wedge dependent propagation parameters: (a) The real part of effective mode refractive index (b) Normalized mode area (c) Propagation length (d) Figure of merit.

To further elucidate the influence of the inter-Si gap height on the propagation characteristics of the 3D DSM-based hybrid plasmonic waveguide, Fig. 9 presents the corresponding mode field distributions at 1.5 THz and 3 THz under varying gap heights. With the Si wedge in the dielectric ridge kept fixed, increasing the gap height progressively drives a larger fraction of the hybrid mode into the cylindrical Si fiber and the supporting SiO_2 medium. Figs. 9(a)-(c) show the mode profiles at f = 1.5 THz for g = 0.5, 1, and 5 μm, yielding effective mode indices of $2.57 + 3.05\times10^{-3}$i, $2.54 + 2.76\times10^{-3}$i, and $2.41 + 1.59\times10^{-3}$i, respectively. Figs. 9(d)-(f) show the mode patterns at f=3 THz. Owing to the markedly reduced permittivity of the 3D DSM at this higher frequency, the dielectric mode dominates within the waveguide, the plasmonic contribution weakens, the confinement of the hybrid mode is diminished, and the

energy progressively concentrates within the Si fiber. This trend becomes increasingly pronounced at elevated frequencies.

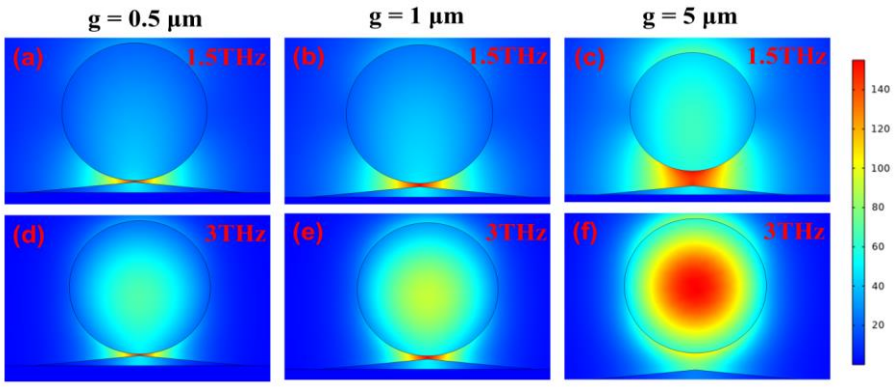


Fig.9 The separation (g=0.5, 1, and 5 μm) dependent mode field distributions at the working frequency of: (a)-(c) 1.5 THz. (d)-(f) 3 THz.

Fig. 10 presents the one-dimensional electric-field energy profiles of the 3D DSM hybrid waveguide under various gap heights, corresponding to the mode field distributions shown earlier. Fig. 10(a) shows the electric-field intensity along the x-direction. As the gap height increases, the peak intensity decreases markedly, and the mode profile broadens around the symmetry center of the hybrid plasmonic waveguide. Along the y-direction, the peak electric field remains located at y=3 μm (the tip of the wedge), yet its magnitude drops substantially as the gap height increases. Moreover, the electric-field energy is uniformly distributed between the cylindrical Si waveguide and the wedge, broadening with increasing gap height owing to the weakened interaction between the plasmonic and dielectric modes. These results demonstrate that maximizing field enhancement and mode confinement of the hybrid plasmonic mode requires minimizing the separation between the Si fiber and the wedge.

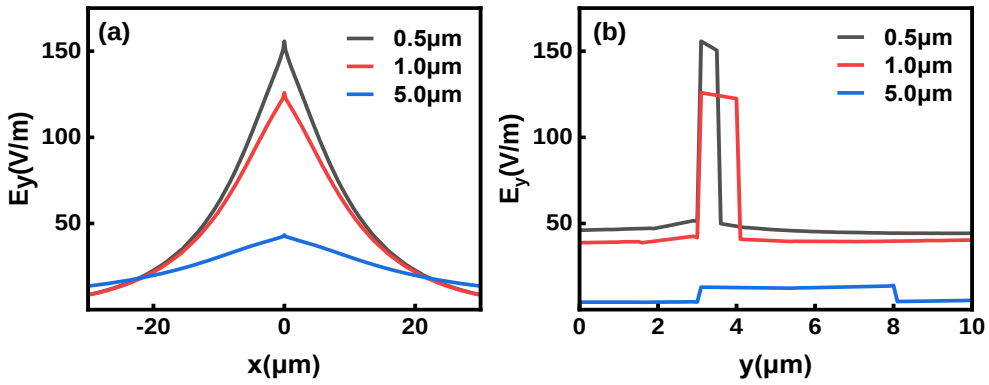


Fig.10 The separation (g=0.5, 1, and 5 μm) dependent electric field intensity distribution along: (a) The x-direction at y=3 μm. (b) The y-direction at x=0 μm.

The Fermi energy and complex permittivity of the 3D DSM can be dynamically tuned via an external bias voltage or by varying the ambient temperature, thereby changing the propagation characteristics of the terahertz waveguide. Fig.11 summarizes the evolution of the waveguide propagation properties when the Fermi energy is swept from 0.03 eV to 0.15 eV. As the Fermi energy increases, the real part of the effective mode index of the hybrid plasmonic mode decreases while the normalized mode area increases. This phenomenon originates from the larger permittivity and stronger metallic response of the 3D DSM at a higher Fermi energy for a fixed frequency. At the frequency of 2 THz, the complex permittivity are $-646+1.18\times10^{2}$ i, $-2620+4.67\times10^{2}$i, and $-5910+1.05\times10^{3}$i for E_F=0.05 eV, 0.1 eV, and 0.15 eV, respectively. In this case, the waveguide exhibits better plasmonic characteristics accompanied by a reduced skin depth, and the low-loss dielectric mode becomes dominant, leading to a lower effective mode index and a larger mode area. Figs. 11(c) and 11(d) reveal that both the propagation length and the figure of merit (FOM) increase monotonically with the Fermi energy, owing to the enhanced plasmonic response at elevated Fermi energy. For a single Fermi-level curve, however, the frequency dependence is more intricate. Taking the red curve (0.03 eV) as an example, the skin depth of the 3D DSM increases with frequency, reaching 3.83 μm, 7.28 μm, and 10.50 μm at frequencies of 1 THz, 2 THz, and 3 THz, respectively. Consequently, a larger fraction of the mode leaks to the 3D DSM layer, increasing

propagation loss and shortening the propagation length. At a low Fermi energy, the 3D DSM exhibits weak metallicity. As the Fermi energy increases, the elevated carrier concentration strengthens the metallic response and improves the plasmonic characteristic, thereby reducing the skin depth. At the same time, increasing frequency causes the low-loss dielectric mode to dominate the hybrid plasmonic mode, lowering the overall loss and increasing the propagation distance. At low frequency, the longer wavelength weakens waveguide confinement, causing the mode to leak into the supporting dielectric or the surrounding air, which yields large normalized mode areas and propagation lengths. As frequency increases, the confinement improves, leading to an initial decrease followed by an increase in both the mode area and the propagation length, as exemplified by the yellow curve in Fig. 11. Fig. 11(d) shows that the FOM increases monotonically with frequency, corroborating the progressive dominance of the dielectric mode within the hybrid mode. By regulating the Fermi energy, the propagation length and quality factor can be changed over a large range. The modulation depth (MD) is used to measure the modulation range of the tunable waveguide, and its calculation formula is: $MD=(x_{max}-x_{min})/x_{max}\times100\%$. When the operating frequency is 3 THz, the waveguide can achieve propagation length modulation in a wide range of 1.48×10^3 μm to 3.2×10^4 μm in the range of 0.03 eV to 0.15 eV, and its modulation depth reaches 95.38%.

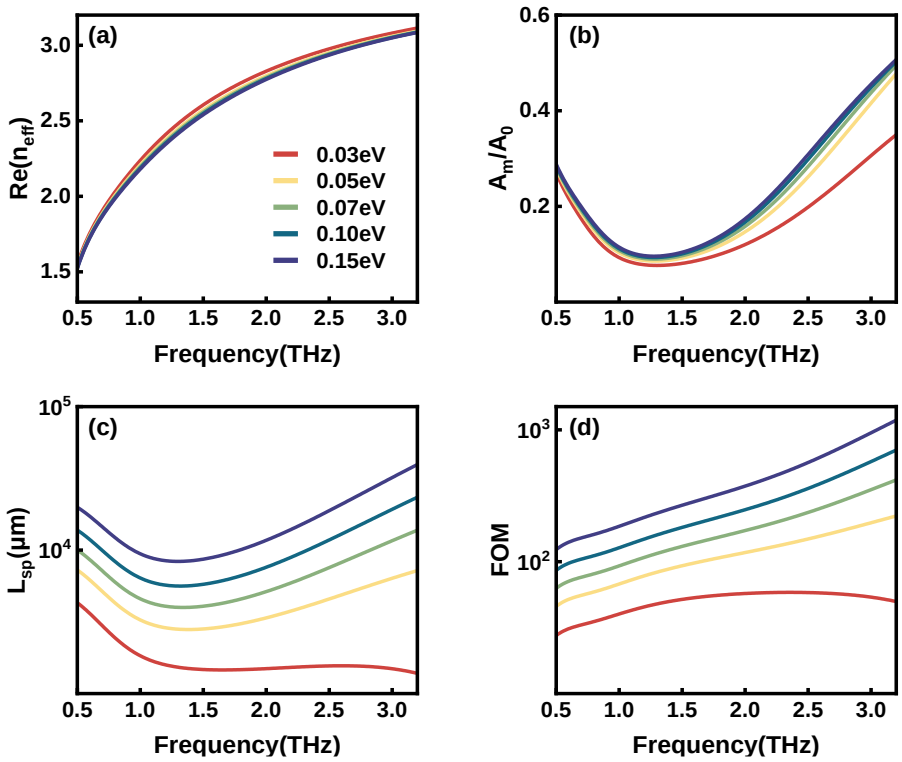


Fig.11 Fermi energy (E_F) dependent propagation parameters: (a) The real part of effective mode refractive index. (b) Normalized mode area. (c) Propagation length. (d) Figure of merit

During the operation of waveguide devices, coupling crosstalk caused by mode field overlap between adjacent waveguides should be taken into consideration, which is of significance for the integration density of optoelectronic devices. In optical waveguide systems, coupling crosstalk is measured by symmetric and antisymmetric modes. In symmetric modes, the electromagnetic field distribution in adjacent waveguides is symmetrical about the center, with the electromagnetic waves propagating in both waveguides having the same phase and low coupling loss. In antisymmetric modes, the electromagnetic field distribution in both waveguides is antisymmetric about the center, with opposite phases and high coupling loss. Crosstalk between adjacent waveguides can be considered negligible when $L/L_{sp}\geq 1$. Here, L_c is coupling length, represented by $L_c=\pi/|\beta_e-\beta_o|$, where β_e and β_o denote the phase propagation constants of the symmetric and antisymmetric supermodes, respectively. L_{sp} is the propagation length when only a single waveguide is

transmitting the electromagnetic wave. Fig. 12 shows the symmetric and antisymmetric modes corresponding to cylindrical Si fibers with different radii r at an operating frequency of 3 THz. S is the distance between the centers of two adjacent Si fibers.

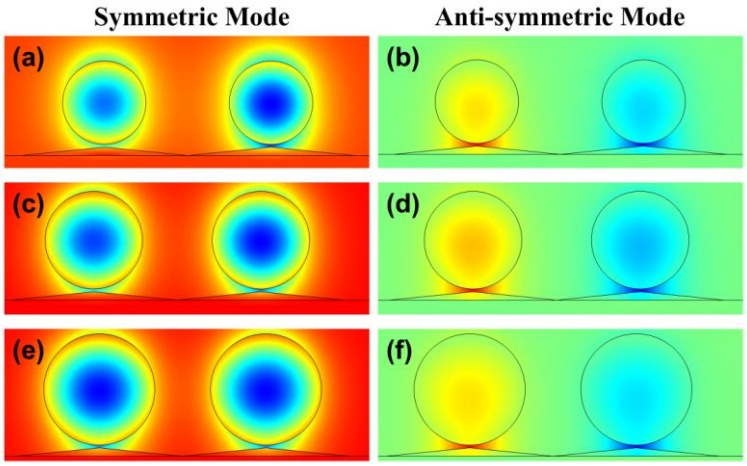


Fig.12 Symmetric mode and anti-symmetric mode for the case of S=60 μm at: (a)-(b) r=15 μm; (c)-(d) r=17.5 μm; (e)-(f) r=20 μm.

Fig. 13 illustrates the dependence of the normalized coupling length L/L_{sp} on the center-to-center separation S for various radius r, revealing an exponential increase of L/L_{sp} with S. For r=15 μm and 17.5 μm, the crosstalk becomes negligible once S exceeds 60 μm, as the cylindrical dielectric radius increases to r=20 μm, a separation greater than 62.5 μm is required to eliminate coupling. These results demonstrate that the reducing cylindrical medium radius suppresses crosstalk at smaller separations, enables denser integration of waveguide elements within a confined footprint and substantially enhancing system capacity and performance. Consequently, optimizing the cylindrical medium radius offers a simple yet effective route for mitigating crosstalk and improving device performance in the design of such photonic structures, providing valuable guidance for the development of efficient, highly integrated THz devices.

For practical implementation, the modal content of the proposed waveguide should also be considered. The presence of higher-order eigenmodes does not necessarily imply multimode interference because modes propagate independently in

a longitudinally uniform waveguide. Multimode interference occurs only when two or more modes are simultaneously excited. In practice, single-mode operation can be ensured through modal-cutoff design, mode-selective excitation, and mode filtering, thereby effectively minimizing the risk of multimode interference [29,30].

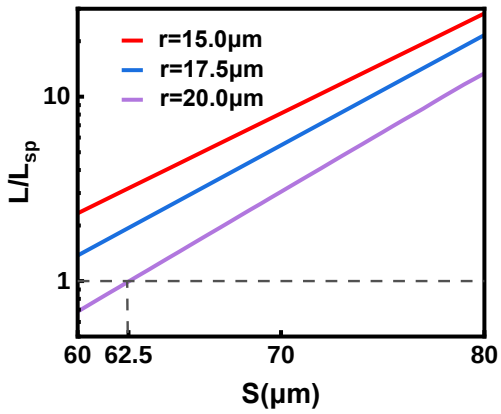


Fig.13 Coupling length versus center-to-center separation *S* under different *r*

4. Conclusion

In this work, we proposed a tunable dielectric ridge hybrid plasmonic waveguide, comprising a cylindrical Si fiber and a wedge-shaped Si segment embedded in a supporting SiO_2 cladding above a 3D DSM layer deposited on a hybrid SiO_2/Si substrate. Using the finite-element analysis method, the propagation characteristics of the hybrid plasmonic waveguides were systematically investigated in the THz regime, including the influences of wedge geometry, gap height, operating frequency, and Fermi energy. The results reveal that both the shape and length of the wedge exert pronounced effects on the propagation behavior. The extending wedge length enhances mode confinement yet simultaneously increases propagation loss, whereas the enlarging inter-dielectric gap height monotonically reduces the real part of the effective mode index while raising the mode area, the propagation length, and the figure of merit. By changing the Fermi energy from 0.03 eV to 0.15 eV, the propagation length of the hybrid mode can be dynamically tuned over a broad range with a modulation depth exceeding 95%. Moreover, crosstalk between adjacent waveguides becomes negligible when their center-to-center separation exceeds 60 μm, and further reduction of the cylindrical Si fiber radius allows this decoupling distance

to be shortened. These findings pave the understanding of the tuning mechanisms in 3D DSM hybrid plasmonic waveguides and provide valuable guidance for the design of highly integrated THz photonic devices.

Declaration of competing interest

The authors declare that they have no known competing financial interests or personal relationships that could have appeared to influence the work reported in this paper.

Acknowledgement

This work was supported by National Key R&D Program of China (No. 2023YFB3210300), the National Natural Science Foundation of China (Grant Nos. 62205131, 12333012), the Natural Science Foundation of Jiangsu Province (BK20220519, BK20240838), and Zhenjiang key laboratory of Advanced Manufacturing of Aerospace Components (SS2023009).

Data availability statement

Data will be made available on request.

References

[1] Islam M S, Cordeiro C M B, Franco M A R, Sultana J, Cruz A L S and Abbott D 2020 *Opt. Express* **28** 16089

[2] Koch M, Mittleman D M, Ornik J and Castro-Camus E 2023 *Nat. Rev. Methods Primers* **3** 48

[3] Yan Z, Zhu L G, Meng K, Huang W and Shi Q 2022 *Trends Biotechnol.* **40** 816

[4] You X H, Wang C X, Huang J, et al. 2021 *Sci. China Inf. Sci.* **64** 110301

[5] Chen H, Yang S, Wang S, Guo H, Wang T, Hu M, Jin B, Wu J, Fang G and Chen X 2025 *Optica* **12** 105

[6] Tong Y, Ding L, Han K, Zou X, Wang S, Wen Z, Ye Y and Ren X 2022 *Food Addit. Contam. Part A* **39** 1555

[7] Mao H P, Du X X, Yan Y T, Zhang X D, Ma G X, Wang Y F, Liu Y, Wang B, Yang X Y and Shi Q 2022 *Int. J. Agric. Biol. Eng.* **15** 180

[8] Lyu J, Huang L, Chen L, Zhu Y and Zhuang S 2024 *Photon. Res.* **12** 194

[9] Zhang X, Xu Q, Xia L, Li Y, Gu J, Tian Z, Ouyang C, Han J and Zhang W 2020 *Adv. Photonics* **2** 014001

[10] Wu C H, Ku C J, Yu M W, Yang J H, Wu P Y, Huang C B, Lu T C, Huang J S, Ishii S and Chen K P 2023 *Adv. Sci.* **10** 2302707

[11] Cheng Y, Cao W H, Wang G Q, He X Y, Lin F T and Liu F 2023 *Opt. Express* **31** 17201

[12] Gadalla M N, Chaudhary K, Zgrabik C M, Capasso F and Hu E L 2020 *Opt. Express* **28** 14536

[13] Cui T, Shen Y, Cheng A, Zhan R, Zheng Z, Tian B, Shi J, Ke Y, Shao L, Chen H and Deng S 2023 *Nanophotonics* **12** 4185

[14] Deng H, Ye F, Malomed B A, Chen X and Panoiu N C 2015 *Phys. Rev. B* **91** 201402(R)

[15] Deng H, Chen X, Malomed B A, Panoiu N C and Ye F 2016 *IEEE J. Sel. Top. Quantum Electron.* **22** 5000509

[16] Kou Y, Ye F and Chen X 2011 *Opt. Express* **19** 11746

[17] Huang C C and Huang C C 2023 *Adv. Photonics Res.* **4** 2200287

[18] Yuan K and Ye L 2024 *IEEE J. Sel. Top. Quantum Electron.* **30** 8600109

[19] Liang T, Gibson Q, Ali M N, Liu M, Cava R J and Ong N P 2015 *Nat. Mater.* **14** 280

[20] Wang G Q, Cao W H and He X Y 2023 *IEEE J. Sel. Top. Quantum Electron.* **29** 8400207

[21] Suo P, Yan S, Pu R, Zhang W, Li D, Chen J, Fu J, Lin X, Miao F, Liang S J, Liu W and Ma G 2022 *Photon. Res.* **10** 653

[22] Wang C L, Han Z H, Hou X, Shao Y S, Deng F Z, Cheng K K, Li Y C, Ma K, Ma Y M, Zhang H Y, Liu M and Zhang Y P 2026 *Chin. Phys. B* **35** 034207

[23] Dai Z, Manjappa M, Yang Y, Tan T C W, Qiang B, Han S, Wong L J, Xiu F, Liu W and Singh R 2021 *Adv. Funct. Mater.* **31** 2011011

[24] Wang J K, Jiang L, Yang X F and Zhao J H 2026 *Chin. Phys. B* **35** 014209

[25] Kotov O V and Lozovik Yu E 2016 *Phys. Rev. B* **93** 235417

[26] Chen H, Zhang H, Liu M, Zhao Y, Guo X and Zhang Y 2017 *Opt. Mater. Express* **7** 3397

[27] He X, Liu F, Lin F and Shi W 2021 *Opt. Lett.* **46** 472

[28] Oulton R F, Sorger V J, Genov D A, Pile D F P and Zhang X 2008 *Nat. Photonics* **2** 496

[29] Colanduoni J, Nikolov D and Xu H 2016 *Plasmonics* **11** 763

[30] Chang K H, Lin Z H, Lee P T and Huang J S 2023 *Sci. Rep.* **13** 5020